Global modes and coupled modes for integrated twin circular-side octagon microlasers

Ke YANG[1,2], Yuede YANG[1,2], Youzeng HAO[1,2], Jiliang WU[1,2], Yongtao HUANG[1,2], Jiachen LIU[1,2], Jinlong XIAO[1,2]* & Yongzhen HUANG[1,2]

[1]*State Key Laboratory of Integrated Optoelectronics, Institute of Semiconductors, Chinese Academy of Sciences, Beijing 100083, China;*
[2]*Center of Materials Science and Optoelectronics Engineering, University of Chinese Academy of Sciences, Beijing 100049, China*

Abstract   Whispering-gallery mode (WGM) microlasers are potential light sources for photonic integrated circuits and optical information processing. In this paper, an integrated twin circular-side octagon microlaser (TCOM) composed of two identical circular-side octagon microcavities (COMs) is proposed and demonstrated for realizing lasing mode control. In a TCOM, we found a global mode with the mode field of an "8" pattern (labeled "8" mode) in addition to weak coupling modes of traditional four-bounce modes. The "8" mode belongs to the whole coupled cavity and is insensitive to the refractive index offset of coupled COMs, but the weak coupling modes are strongly sensitive to the refractive index offset. Lasing mode transformation from multiple coupled modes to a single "8" mode is demonstrated by adjusting the refractive index offset through injection currents. Weak coupling modes for directly connected TCOMs and lasing mode control make the COM a potential unit for large-scale photonic integration and optical information processing.

Keywords   optical microcavity, semiconductor lasers, coupled cavity, lasing mode control, photonic integration

1   Introduction

On-chip interconnects and photonic integration technologies for short-distance communications are the inevitable trend for the development of information technology in the future. Whispering-gallery mode (WGM) microlasers are ideal potential light sources for single nanoparticle detection, microwave photonics, large-scale integration, and optical information processing owing to the advantages of the high quality (Q) factor, small mode volume, low power consumption, and integration potential [1–9]. There are many laser schemes for large scale photonic integration for information processing. Supersymmetric microring laser arrays have been demonstrated to support super-mode lasing corresponding to two nearby longitudinal orders by harnessing notions from SUSY quantum mechanics, which paves the way towards large-scale SUSY laser array design on the same chip [10]. Stable-longitudinal mode operation has been investigated in a system of coupled microring lasers by harnessing notions from PT symmetry. The scheme features inherently self-adapting and facilitates mode selectivity over a broad bandwidth without the need for other additional intricate components [11]. Hybrid-cavity lasers consisting of a WGM cavity with large free spectral range and Fabry-Perot (FP) cavity have been demonstrated for mode Q factor control and single-mode operation [12–14]. Recently, coupled-WGM microcavity lasers have been experimentally studied in many aspects. Broken symmetric coupled microcavity lasers are predicted and numerically examined for enhancing modulation [15]. For coupled twin-square microcavity laser, modulation bandwidth enhancement was investigated based on the photon-photon resonance effect [16]. An integrated twin-microdisk laser, as a seeding source, was used to generate a multi-coherence
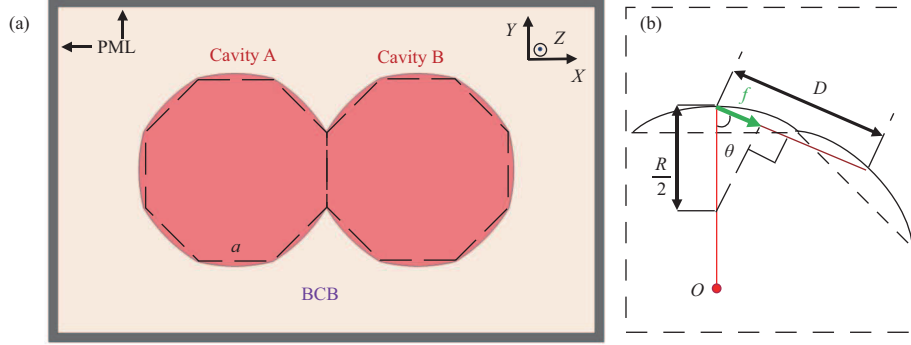

Figure 1 (Color online) Schematic diagram of (a) the simulated twin-circular-side-octagon microlasers composed of two identical circular-side octagon microcavities by the FEM simulation and (b) two adjacent circular-sides of a COM.

wavelength source [17]. Photonic microwave generation was achieved using an integrated twin-microdisk laser [18]. Coupled lasers were demonstrated in achieving stable single-mode operation using parity-time symmetry [11, 19]. In addition, different types of coupled cavities based on the Vernier effect, such as etched or cleaved coupled-cavity lasers [20–22], coupled-ring lasers [23, 24], Y-branch lasers [25], as well as V-coupled lasers [26, 27], were applied to realize single-mode lasing.

In this paper, we propose an integrated twin circular-side octagon microlaser (TCOM) consisting of two connected circular-side octagon microcavities (COMs) and demonstrate lasing mode control. The introduction of the circular sides enhances the mode Q factor for the four-bounce mode to the order of 10^8, owing to the light-ray-converging effect of the concave mirrors [28]. The circular sides can converge the mode light rays along a narrow transmission path and reduce the scattering loss at the vertices. The strong mode confinement is versatile that can be used for photonic integration with intrinsic weak coupling even for integrated-WGM microcavity laser. In addition to weakly coupling modes, we find a global "8" mode belonging to whole coupled cavities, which is insensitive to the refractive index offset between the two COMs. However, mode characteristics of coupled four-bounce modes are sensitive to the refractive index offset. Hence, the "8" mode of the whole coupled cavities and the weak coupling four-bounce modes provide a new mechanism for the implementation of lasing mode control.

This paper is organized as follows. Section 2 introduces the device structure and the simulation results of TCOMs. Section 3 experimentally analyzes and illustrates the multi-mode lasing with injecting current to only a COM, as well as lasing mode transformation from multiple modes to single "8" mode operation for TCOMs. Section 4 gives a summary and conclusion.

2 Device structure and simulation

A TCOM consisting of two identical COM integrated is considered by connecting one side of the COMs as shown in Figure 1(a). The geometry of a COM is determined by the flat-side of a and the deformation degree M. Figure 1(b) illustrates the schematic diagram of two adjacent sides of a COM, where D, R, θ, and f are the distance between the midpoints of adjacent sides, the radius of the circular side, the incident angle of the light ray propagating along the line connecting the midpoints of adjacent sides, and the focal length along the line connecting the midpoints of adjacent sides, respectively [28]. The focal length f is therefore described as $f = R \cos \theta / 2$, and the deformation degree M is defined as $M = D/f$. A two-dimensional (2D) finite element method (FEM) (COMSOL Multiphysics) is used to investigate the mode characteristics of the TCOM. The practical devices are InP-based and laterally surrounded by bisbenzocyclobutene (BCB), and the effective refractive indices of the cavities and the BCB medium are taken to 3.2 and 1.54, respectively. A perfect matched layer (PML) absorbing boundary with a width of 1.5 μm is used to terminate the simulation window, and the maximum grid size with one-sixth of the mode wavelength is set to ensure the accuracy of the computation. The structure parameters are taken to be $a = 15$ μm and $M = 1.5$.

We first simulate mode characteristics for cavity B as a nearly isolated cavity by setting cavity A as a loss cavity with the imaginary part of the refractive index $\Delta \text{Im}(n_A)$ of 2×10^{-3}. The obtained Q factors versus the mode wavelengths ranging from 1550 to 1560 nm for transverse electric (TE) modes are shown in Figure 2(a). There are five high-Q TE modes with Q factors larger than 10^4, owing to the light
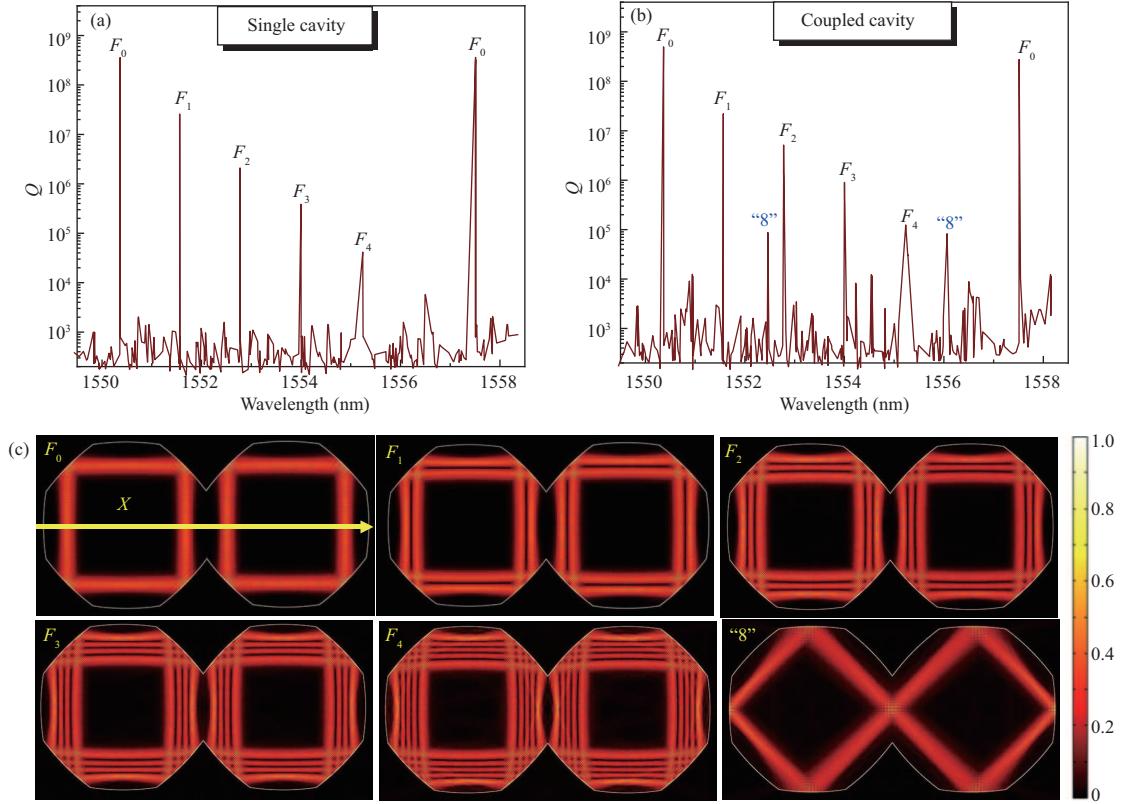
Figure 2 (Color online) Mode Q factors versus the variation of mode wavelengths for a TCOM with $a = 15$ μm and $M = 1.5$ for (a) $\Delta\mathrm{Im}(n_\mathrm{A}) = 2 \times 10^{-3}$ and $\Delta\mathrm{Im}(n_\mathrm{B}) = 0$, (b) $\Delta\mathrm{Im}(n_\mathrm{A}) = \Delta\mathrm{Im}(n_\mathrm{B}) = 0$, respectively. (c) Magnetic field ($|\mathrm{Hz}|$) of the modes F_0, F_1, F_2, F_3, F_4, and "8" mode at $\Delta\mathrm{Im}(n_\mathrm{A}) = \Delta\mathrm{Im}(n_\mathrm{B}) = 0$, respectively.

confinement effect of the concave mirrors, which are marked as F_0, F_1, F_2, F_3, and F_4, representing the four-bounce modes of the fundamental transverse mode, the first-order mode, the second-order mode, the third-order mode, and the fourth-order mode, respectively. The wavelengths of F_0 mode are 1550.33 and 1557.50 nm, with corresponding Q factors of 4.9×10^8 and 2.8×10^8. Mode Q factors are $2.2 \times 10^7, 3.6 \times 10^6, 3.5 \times 10^5$, and 3.3×10^4 for F_1, F_2, F_3, and F_4 at the wavelengths of 1551.57, 1552.78, 1554.00, and 1555.23 nm, respectively. The mode wavelength intervals of the adjacent four-bounce modes F_0, F_1, F_2, F_3, and F_4 are 1.24, 1.21, 1.22, and 1.23 nm, respectively.

For both microcavities in the same condition with $\Delta\mathrm{Im}(n_\mathrm{A}) = \Delta\mathrm{Im}(n_\mathrm{B}) = 0$, we can calculate mode field patterns and mode Q factors for the symmetric TCOM. The mode Q factors versus mode wavelengths are presented in Figure 2(b) with the corresponding magnetic field distribution $|\mathrm{Hz}|$ in Figure 2(c). The mode Q factors of F_0, F_1, F_2, F_3, and F_4 are in order of $10^8, 10^7, 10^6, 10^5$, and 10^4, respectively, which are in the same magnitude as those in Figure 2(a). For the fundamental and the first-order transverse modes F_0 and F_1, we still can obtain mode field patterns as an isolated COM, i.e., without mode coupling owing to near zero overlap between the modes confined in the cavities A and B. Four nondegeneracy coupled modes exist for F_2, F_3, and F_4, with symmetric and anti-symmetric concerning the x-axis and the coupled side, respectively. Remarkably, we find another set of high-Q modes marked by "8" in Figure 2(b), with the mode field pattern of "8" in Figure 2(c). The mode wavelengths of the "8" modes are 1552.5 and 1556.1 nm, with corresponding Q factors of 8.7×10^4 and 8.4×10^4. The optical path of the "8" mode is twice that of the four-bounce mode with a longitudinal-mode wavelength interval of 3.6 nm, which is half of that (7.2 nm) of the four-bounce mode.

To further study the mode characteristics of the four-bounce modes and "8" mode, we calculate the mode wavelengths of the $F_{0\mathrm{A}}$ mode and the "8" mode versus $\Delta\mathrm{Re}(n_\mathrm{A})$, the variation of the real refractive index of cavity A. Control of the refractive index can be realized dynamically, e.g., via pump power control [29, 30], changes of the environmental gas [31], or temperature control [32]. As shown in Figure 3(a), the redshift rate of $F_{0\mathrm{A}}$ 5.5 nm/0.01 is about twice that of the "8" mode 2.4 nm/0.01. The refractive index offset induces each four-bounce mode divided into two groups. One group is distributed
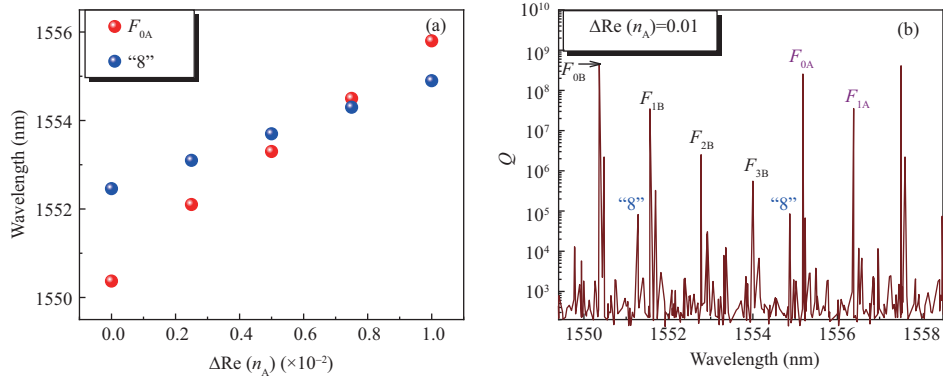
Figure 3 (Color online) (a) Mode wavelengths versus $\Delta\mathrm{Re}(n_A)$ for F_{0A} mode distributed in cavity A and "8" mode. (b) Mode Q factors versus mode wavelengths for the coupled cavity at $\Delta\mathrm{Re}(n_A)= 0.01$. F_{0A} and F_{0B} modes belong to two sets of longitudinal modes, and corresponding magnetic fields ($|Hz|$) are distributed in cavities A and B, respectively.
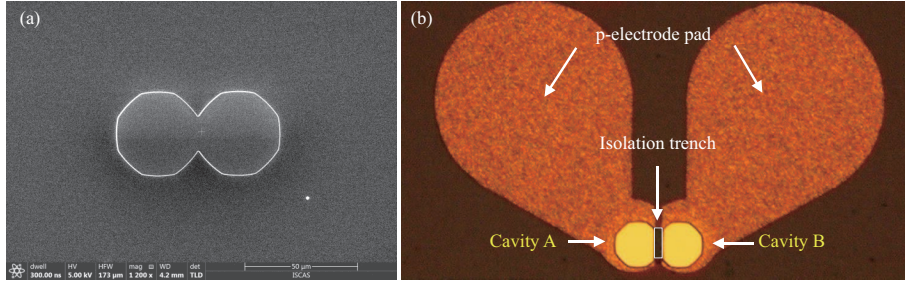

Figure 4 (Color online) (a) SEM image of a twin-circular-side-octagon coupled-cavity after the ICP etching process. (b) Microscopic image of the fabricated TCOM with patterned p-electrodes for current injection into two cavities separately.

in cavity A and redshifts with $\Delta\mathrm{Re}(n_A)$, while the other group is distributed in cavity B with near unchanged wavelengths. Therefore, the refractive index offset induces two sets of free spectrum ranges for four-bounce modes. But the magnetic field ($|Hz|$) of the "8" mode is robust to the refractive index offset and distributes near uniform between the two coupled cavities, in fact as a whole cavity as shown in Figure 2(c). The "8" mode at 1552.5 nm with $\Delta\mathrm{Re}(n_A) = 0$ redshifts to 1554.9 nm with $\Delta\mathrm{Re}(n_A) = 0.01$. Consequently, the coupled four-bounce modes are destroyed with the increase of refractive index offset and become modes of an isolated cavity, while the "8" mode can exist more stably. Figure 3(b) shows Q factors of the coupled cavity versus the mode wavelengths ranging from 1550 to 1560 nm for all modes at $\Delta\mathrm{Re}(n_A) = 0.01$. F_{0B} mode at 1550.3 nm and F_{0A} mode at 1555.8 nm belong to two different groups of longitudinal modes, and their corresponding mode field patterns distribute in cavities B and A, respectively.

3 Experimental results

The TCOMs are fabricated using an AlGaInAs/InP laser wafer with the active region of compressively strained multiple quantum wells (MQWs), grown on n-doped In-P substrate by metal-organic chemical vapor deposition. A SiO$_2$ layer is deposited using plasma-enhanced chemical vapor deposition (PECVD), and then standard contacting photolithography and inductively coupled plasma (ICP) etching techniques are employed to form the coupled cavity with a deep etching depth of about 4 μm. The scanning electron microscope (SEM) image is shown in Figure 4(a) for the coupled cavities after ICP etching process, which shows smooth circular sides. The coupled-cavity is laterally confined by a BCB layer for planarization. Afterward, an isolation trench with a width of 4 μm is carved by ICP etching the p-InGaAs ohmic contact layer off between both microcavities for guaranteeing mutual electrical isolation [12, 14]. A p-electrode pad is deposited by e-beam evaporation and lift-off process, and an n-electrode pad is completed after mechanically lapping down to a thickness of about 120-μm. The microscope image of a fabricated TCOM is shown in Figure 4(b) after the deposition of the P-type and N-type electrodes. The TCOM laser with $a = 15$ μm and $M = 1.5$, the same as that used in the numerical simulation, is mounted on an AlN
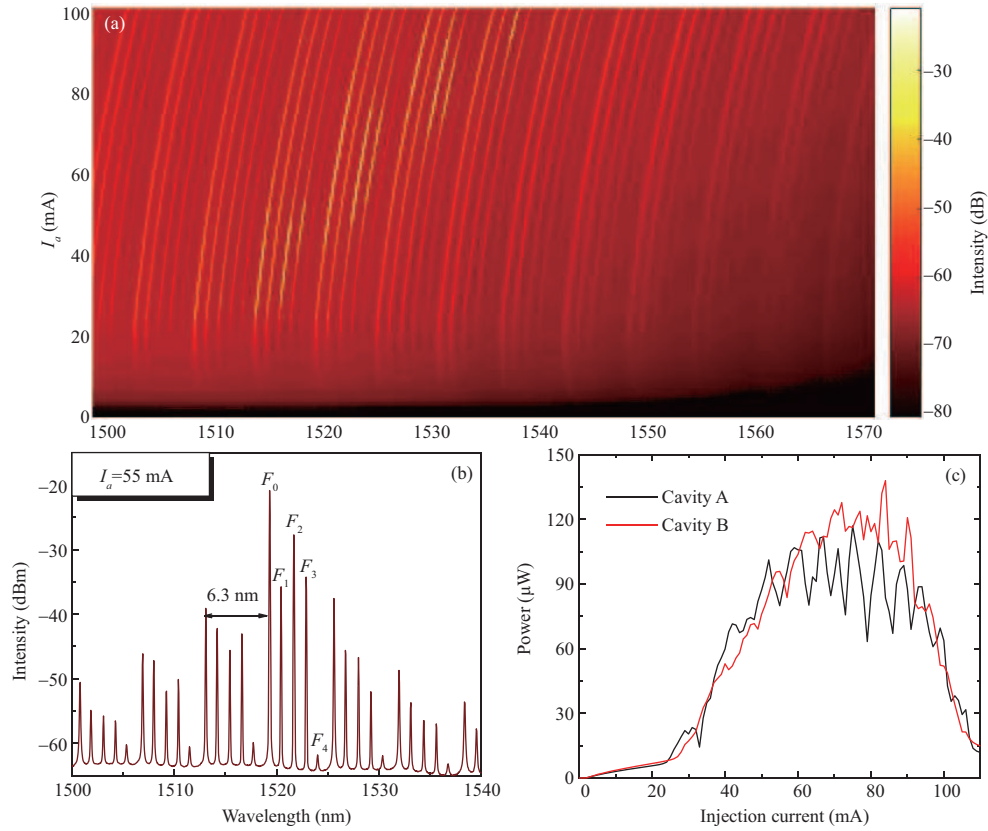
Figure 5 (Color online) (a) Lasing spectra of cavity A in a separate operating state with the multi-mode fiber located near cavity A. (b) The detailed lasing spectra of cavity A at an injection current of $I_a = 55$ mA. (c) Output power coupled into a multi-mode fiber versus injection current of cavities A and B at 291 K, respectively.

sub-mount for testing.

We first studied the static characteristics of cavity A of the TCOM by measuring lasing spectra using an optical spectrum analyzer (OSA) with a resolution of 0.02 nm, with a continuous-wave (CW) injection current I_a applied to cavity A. As shown in Figure 5(a), the lasing spectra of the free-running cavity A show multi-mode lasing, owing to the high Q factors of the lasing modes. Similarly, the phenomena of multi-longitudinal-transverse mode lasing were observed in cavity B by only applying current to cavity B with the multi-mode fiber located near cavity B. Figure 5(b) illustrates the detailed lasing spectra of cavity A at I_a of 55 mA. There are six groups of longitudinal modes with the wavelength ranging from 1500 to 1540 nm. Five specific lasing modes in each group of longitudinal modes with wavelengths around 1520 nm are marked with F_0, F_1, F_2, F_3, and F_4, respectively. The wavelengths of modes F_0, F_1, F_2, F_3, and F_4 around 1520 nm are 1519.32, 1520.47, 1521.65, 1522.84, and 1524.02 nm, respectively. The mode wavelength intervals of the adjacent four-bounce modes F_0, F_1, F_2, F_3, and F_4 are 1.15, 1.18, 1.19, and 1.18 nm, respectively, with the experimental-simulation difference of 7.25%, 2.48%, 2.46%, and 4.07%, respectively. The longitudinal-mode interval of 6.3 nm is a little smaller than the simulation results with the same size because a constant effective refractive index of 3.2 is adopted in the simulation, and the effect of dispersion is not taken into account. The relative positions of different modes and the mode wavelength intervals are consistent with the simulation results in Figure 2(a). The output powers of cavities A and B at their free-running state collected by a multi-mode fiber are presented in Figure 5(c), respectively, at the thermoelectric cooler (TEC) temperature of 291 K with CW injection currents applied to cavities A and B separately. The threshold currents of cavities A and B are 22 and 24 mA, respectively, and the corresponding maximum output powers are 137 and 116 μW with the injection currents of 84 and 75 mA.

To investigate the characteristics of the mode coupling for the TCOMs, the injection currents are applied to the two microcavities simultaneously. The lasing spectra with different injection currents I_b and fixed $I_a = 50$ mA are shown in Figure 6(a), as the multi-mode fiber is placed near cavity A. Both single-mode and multi-mode lasing are observed from the lasing spectra, and the insets show the relative
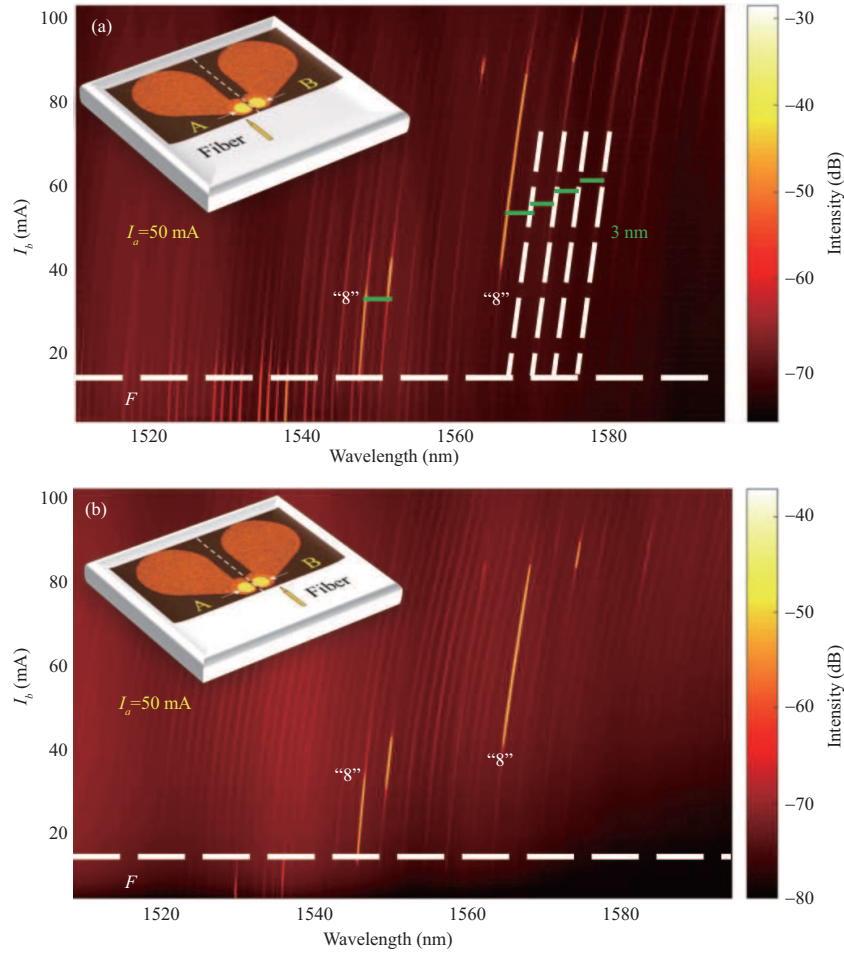
Figure 6 (Color online) Lasing characteristics with the variations of I_b for TCOMs with $a = 15$ μm and $M = 1.5$. Lasing spectra versus I_b with the multi-mode fiber located near (a) cavity A and (b) cavity B at fixed $I_a = 50$ mA. Insets show the placement of the multi-mode fiber. The lasing modes above the white horizontal dashed line are "8" modes, conversely, the lasing modes are F (four-bounce) modes.

position of multi-mode fiber to the actual TCOM. The four-bounce modes lase as I_b increases from 0 to 11 mA. The "8" mode starts to lase and four-bounce modes are suppressed almost at the same time as I_b increases to above 12 mA, marked by the white horizontal dashed line. Although the four-bounce modes have high Q factors, they have weak coupling characteristics and are extremely sensitive to the refractive index offset between two cavities. Therefore, the "8" mode distributed in the whole cavity consumes a large number of injected carriers and suppresses the lasing of four-bounce modes. The "8" mode lasing mode redshifts from 1544 to 1545.3 nm as I_b increases from 12 to 32 mA, and hops to 1548.4 nm at $I_b = 33$ mA with about one longitudinal mode interval for the "8" mode of around 3 nm. The dominant mode hops from 1548.8 to 1564.2 nm at $I_b = 42$ mA with about five times as much as the longitudinal mode interval for the "8" mode. The trajectories and longitudinal mode interval for "8" modes are indicated by white dashed lines with the same slope of 0.07 nm/mA and green solid lines with a width of 3 nm, respectively. Moving the fiber near cavity B and keeping other conditions unchanged, we measure the lasing spectra versus I_b at fixed $I_a = 50$ mA, as shown in Figure 6(b). The intensities of the four-bounce modes are very weak owing to the scattered light from cavity A as $I_b < 12$ mA, i.e., they are mainly located in cavity A as shown in Figures 6(a) and (b). However, the intensities of the lasing modes are obviously close to that of cavity A as $I_b > 12$ mA, which further verifies that the lasing mode is "8" mode.

The dominant lasing mode wavelengths and corresponding side mode suppression ratios (SMSRs) are illustrated in Figure 7(a) for the TCOM versus I_b at $I_a = 55$ mA. The "8" mode redshifts from 1566.6 to 1570.0 nm as I_b increases from 58 to 105 mA. The lasing mode redshifts with the increase of I_b, owing to the change of the refractive index caused by the thermal effect [14]. The lasing mode hops at $I_b =$
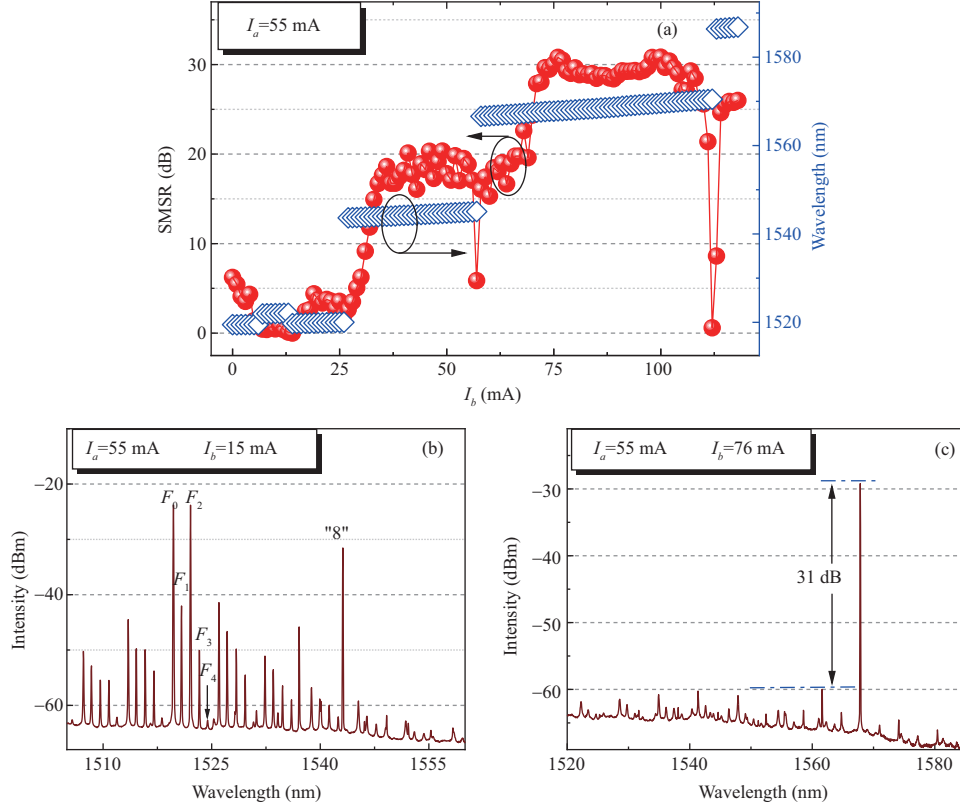
Figure 7 (Color online) (a) Dominant lasing mode wavelengths and corresponding SMSRs versus I_b with the multi-mode fiber located near cavity A at fixed $I_a = 55$ mA. The detailed lasing spectra with (b) $I_b = 15$ mA and (c) $I_b = 76$ mA.

58 mA, owing to the redshift of gain spectra. Stable single-mode operation with SMSRs over 28 dB is observed with I_b increased from 70 to 105 mA. When cavity B is at a low injection current, multi-mode lasing of four-bounce modes is observed. In order to describe the lasing process more specifically, the lasing spectra are illustrated in Figure 7(b) at $I_b = 15$ mA. The wavelengths of modes F_0, F_1, F_2, F_3, and F_4 in the same group of longitudinal modes are 1519.72, 1520.88, 1522.08, 1523.28, and 1524.45 nm with mode wavelengths of adjacent transverse modes of 1.16, 1.20, 1.20, and 1.17 nm, respectively, and the wavelength of the lasing "8" mode is at 1543.1 nm. At $I_b = 76$ mA, single mode operation of an "8" mode is realized at 1567.8 nm with the SMSR of 31 dB as shown in Figure 7(c).

4 Conclusion

In conclusion, we have proposed and demonstrated TCOMs for realizing lasing mode control. The numerical simulation results indicate that the refractive index offset induces two sets of free spectrum ranges for four-bounce modes, while the "8" mode is insensitive to the refractive index offset. Multi-mode lasing is presented with independently running for both COMs, which agrees well with the numerical analysis. Detailed experimental results prove that lasing mode transformation from multiple-mode to single "8" mode with an SMSR up to 31 dB by adjusting injection currents for TCOM. Moreover, the "8" mode belonging to the whole coupled-cavity can achieve stable lasing over a wide injection current range. The "8" mode and the weak coupling four-bounce modes provide a new mechanism for the implementation of lasing mode control. We believe that the COMs have broad prospects as a potential light source for large-scale integration and optical information processing.

References

1 McCall S L, Levi A F J, Slusher R E, et al. Whispering-gallery mode microdisk lasers. Appl Phys Lett, 1992, 60: 289–291
2 Vahala K J. Optical microcavities. Nature, 2003, 424: 839–846

3   Roelkens G, Liu L, Liang D, et al. III-V/silicon photonics for on-chip and intra-chip optical interconnects. Laser Photon Rev, 2010, 4: 751–779

4   Cao H, Wiersig J. Dielectric microcavities: model systems for wave chaos and non-Hermitian physics. Rev Mod Phys, 2015, 87: 61–111

5   Yang S C, Wang Y, Sun H D. Advances and prospects for whispering gallery mode microcavities. Adv Opt Mater, 2015, 3: 1136–1162

6   Kryzhanovskaya N V, Moiseev E I, Zubov F I, et al. Direct modulation characteristics of microdisk lasers with InGaAs/GaAs quantum well-dots. Photon Res, 2019, 7: 664–668

7   Liu Z, Xu Y, Lin Y, et al. High-Q quasibound states in the continuum for nonlinear metasurfaces. Phys Rev Lett, 2019, 123: 253901

8   Calabrese A, Ramiro-Manzano F, Price H M, et al. Unidirectional reflection from an integrated "taiji" microresonator. Photon Res, 2020, 8: 1333–1341

9   Jiang X F, Zou C L, Wang L, et al. Whispering-gallery microcavities with unidirectional laser emission. Laser Photonics Rev, 2016, 10: 40–61

10   Midya B, Zhao H, Qiao X D, et al. Supersymmetric microring laser arrays. Photon Res, 2019, 7: 363–367

11   Hodaei H, Miri M A, Heinrich M, et al. Parity-time-symmetric microring lasers. Science, 2014, 346: 975–978

12   Ma X W, Huang Y Z, Yang Y D, et al. Mode and lasing characteristics for hybrid square-rectangular lasers. IEEE J Sel Top Quantum Electron, 2017, 23: 1–9

13   Huang Y Z, Ma X W, Yang Y D, et al. Hybrid-cavity semiconductor lasers with a whispering-gallery cavity for controlling Q factor. Sci China Inf Sci, 2018, 61: 080401

14   Hao Y Z, Wang F L, Tang M, et al. Widely tunable single-mode lasers based on a hybrid square/rhombus-rectangular microcavity. Photon Res, 2019, 7: 543–548

15   Xu C, Hayenga W E, Hodaei H, et al. Enhanced modulation characteristics in broken symmetric coupled microring lasers. Opt Express, 2020, 28: 19608

16   Xiao Z X, Huang Y Z, Yang Y D, et al. Modulation bandwidth enhancement for coupled twin-square microcavity lasers. Opt Lett, 2017, 42: 3173–3176

17   Weng H Z, Huang Y Z, Xiao J L, et al. Multicoherence wavelength generation based on integrated twin-microdisk lasers. Opt Lett, 2016, 41: 5146–5149

18   Zou L X, Liu B W, Lv X M, et al. Integrated semiconductor twin-microdisk laser under mutually optical injection. Appl Phys Lett, 2015, 106: 191107

19   Kominis Y, Choquette K D, Bountis A, et al. Exceptional points in two dissimilar coupled diode lasers. Appl Phys Lett, 2018, 113: 081103

20   Coldren L A, Miller B I, Iga K, et al. Monolithic two-section GaInAsP/InP active-optical-resonator devices formed by reactive ion etching. Appl Phys Lett, 1981, 38: 315–317

21   Tsang W T, Olsson N A, Logan R A. High-speed direct single-frequency modulation with large tuning rate and frequency excursion in cleaved-coupled-cavity semiconductor lasers. Appl Phys Lett, 1983, 42: 650–652

22   Ebeling K J, Coldren L A, Miller B I, et al. Single-mode operation of coupled-cavity GaInAsP/InP semiconductor lasers. Appl Phys Lett, 1983, 42: 6–8

23   Matsuo S, Segawa T. Microring-resonator-based widely tunable lasers. IEEE J Sel Top Quantum Electron, 2009, 15: 545–554

24   Segawa T, Kobayashi W, Sato T, et al. A flat-output widely tunable laser based on parallel-ring resonator integrated with electroabsorption modulator. Opt Express, 2012, 20: B485

25   Kuznetsov M, Verlangieri P, Dentai A G. Frequency tuning characteristics and WDM channel access of the semiconductor three-branch Y3-lasers. IEEE Photon Technol Lett, 1994, 6: 157–160

26   Zhang S, Meng J J, Guo S L, et al. Simple and compact V-cavity semiconductor laser with 50×100 GHz wavelength tuning. Opt Express, 2013, 21: 13564–13571

27   Zhuang Y, Li Q L, Yang Y Q, et al. Transmission distance extension of directly modulated tunable V-cavity laser using AWG wavelength detuning. IEEE Photonics J, 2020, 12: 1–7

28   Tang M, Yang Y D, Weng H Z, et al. Ray dynamics and wave chaos in circular-side polygonal microcavities. Phys Rev A, 2019, 99: 033814

29   Bennett B R, Soref R A, Alamo J A D. Carrier-induced change in refractive index of InP, GaAs and InGaAsP. IEEE J Quantum Electron, 1990, 26: 113–122

30   Hayat A, Tong J H, Chen C, et al. Multi-wavelength colloidal quantum dot lasers in distributed feedback cavities. Sci China Inf Sci, 2020, 63: 182401

31   Vollmer F, Yang L. Review label-free detection with high-Q microcavities: a review of biosensing mechanisms for integrated devices. Nanophotonics, 2012, 1: 267–291

32   Benyoucef M, Shim J B, Wiersig J, et al. Quality-factor enhancement of supermodes in coupled microdisks. Opt Lett, 2011, 36: 1317–1319